Supporting Information for

Structural origin of relaxation in dense colloidal suspensions

Ratimanasee Sahu, Mohit Sharma, Peter Schall, Sarika Maitra Bhattacharyya, Vijayakumar Chikkadi

To whom correspondence should be addressed. E-mail: mb.sarika@ncl.res.in; vijayck@iiserpune.ac.in

This PDF file includes:

Supporting text
Figs. S1 to S15
SI References

Contents

1 Calculation of structural order parameter from the mean-field caging potential **3**
A Calculation of global structural order parameter S^{av} . . . 3
B Structural order parameter in the real space . . . 3
C Calculation of local structural order parameter . . . 5

2 Structural order parameter of rearranging particles in bidisperse colloidal monolayer **6**

3 Structural order parameter dependent probability of rearrangements. **6**
A Comparison of different methods used for calculating P_R . . . 6
B $P_R(S)$ for full range of SOP values . . . 7
C Effect of thresholding on $P_r(S)$ in quiescent systems . . . 8
D Effect of thresholding on $P_r(S)$ in sheared systems . . . 8

4 Structure-dynamics correlations using Spearman rank correlation coefficient **9**
A Spearman rank correlations of quiescent system and effect of coarse-graining SOP . . . 9

5 Scatter plots of SOP and particle displacements **9**

6 Structure and dynamics in sheared systems in 3D **11**

Supporting Information Text

1. Calculation of structural order parameter from the mean-field caging potential

A. Calculation of global structural order parameter S^{av}. We employed the local structural order parameter (SOP), evaluated on a particle level, in the main paper for investigating the correlations of structure and dynamics. The formulation of these concepts follows the derivation of global structural order parameter S^{av} from dynamic density functional theory and mean-field assumptions (1–3). These concepts are outlined in this section.

Following the mean-field theory, we can map the dynamics of a set of interacting particles in terms of the dynamics of a set of non-interacting particles in a potential $\Phi(r)$. The temporal evolution of the average density,

$$\frac{\partial \rho(\mathbf{r},t)}{\partial t} = \nabla \cdot \left[\frac{1}{\xi} \left(k_B T \nabla \rho(\mathbf{r},t) + \rho(\mathbf{r},t) \nabla \Phi(\mathbf{r}) \right) \right], \quad [1]$$

where ξ is the friction coefficient. The effective potential $\Phi(r)$ felt by a particle at r is due to the interaction with the other particles present in the system. This mean-field potential in the DDFT approach is given by $\Phi(r) = \frac{\delta F_{ex}}{\delta \rho}$, where F_{ex} is the excess free energy. Next, following the Ramakrishnan-Yussouff (RY) formalism (4), the excess free energy functional can be written in terms of the equilibrium average density $\rho(q)$ and the direct correlation function $C(q)$ in d-dimensional as

$$\beta F_{ex}(\rho(q)) = -\frac{1}{2} \int \frac{d\mathbf{q}}{(2\pi)^d} \rho(-\mathbf{q},t) C(q) \rho(\mathbf{q},t), \quad [2]$$

where $\beta = \frac{1}{k_B T}$ which is set to unity. To dynamically close the theory in the above expression we use the Vineyard approximation, and we also neglect the self term. Thus the mean-field caging potential Φ_q^{av} felt by a particle can be written as (1, 5),

$$\beta \Phi_q^{av}(\Delta r) = -\int \frac{\mathbf{dq}}{(2\pi)^d} \; C(q) \; [\mathbb{S}(q) - \mathbb{I}] \; e^{\frac{-q^2 \Delta r^2}{2d}}, \quad [3]$$

where Δr is the displacement of a particle from its equilibrium position, $\mathbb{S}(q) = 1/N \sum \exp(-j\mathbf{q}.\mathbf{r})$ is the structure factor and the direct correlation function $C(\mathbf{q}) = \mathbb{I} - \mathbb{S}^{-1}(\mathbf{q})$. The superscript "av" denotes the global quantity that is obtained from the structure factor.

For a n species system, the form of the potential is:

$$\beta {\Phi_q}^{av}(\Delta r) = -\int \frac{\mathbf{dq}}{(2\pi)^d} \sum_{u=1}^{n} \sum_{v=1}^{n} C_{uv}(q) \sqrt{x_u x_v} \times [\mathbb{S}_{uv}(q) - \delta_{uv}] \, e^{\frac{-q^2 \Delta r^2}{2d}}, \quad [4]$$

where the partial structure factor is given by $\mathbb{S}_{uv}(\mathbf{q}) = 1/\sqrt{N_u N_v} \sum_{i=1}^{Nu} \sum_{j=1}^{Nv} \exp[-j\mathbf{q}.(\mathbf{r_i^u} - \mathbf{r_j^v})]$ and x_u, x_v are fractions of u and v particles, respectively. The depth of the potential is given by:

$$\beta {\Phi_q}^{av}(\Delta r = 0) = -\int \frac{\mathbf{dq}}{(2\pi)^d} \sum_{u=1}^{n} \sum_{v=1}^{n} C_{uv}(q) \sqrt{x_u x_v} \times [\mathbb{S}_{uv}(q) - \delta_{uv}] \, . \quad [5]$$

The results presented in this section are for a bidisperse colloidal monolayer with $n = 2$, and for only one species of particles (large particles). The partial structure factor for the quiescent system at two different densities is shown in Fig. S1*A*. The caging potential is shown in Fig. S1*B* for several densities. As the packing fraction increases, the depth of the mean field potential increases as well as the curvature of the potential increases. This suggests that at higher densities, the relaxation time is longer, which is verified in Fig. S1*C*.

The average structural order parameter(SOP) is determined by fitting the potential near $\Delta r = 0$ to a harmonic form $\beta \Phi_q^{av}(\Delta r) = \beta \Phi_q^{av}(\Delta r = 0) + \frac{1}{2} \Delta r^2 / S^{av}$, where $\Phi_q^{av}(\Delta r = 0)$ is the value of the potential at the minima and $\frac{1}{S^{av}}$ is the curvature, which represents the stiffness of the potential. The relationship between the curvature $\frac{1}{S^{av}}$ and the depth of the potential $\Phi_q^{av}(\Delta r = 0)$ is shown in Fig. S1*D*. Note that we always consider $|\Phi_q^{av}(\Delta r = 0)|$ when referring to the depth of the potential. Evidently, their dependence is linear and can be expressed as $\frac{1}{S^{av}} = a_0 + a_1 \Phi_q^{av}(\Delta r = 0)$, where a_0 and a_1 are constants. This implies that the SOP obtained from the depth of the potential and the inverse of its curvature are equivalent. Therefore, we estimate the SOP using the relation: $S^{av} \propto \frac{1}{|\beta \Phi(\Delta r = 0)|}$. We show that as the area-fraction increases, the global structure order parameter decreases, and as a whole the system becomes stiffer, which is displayed in the inset of Fig. S1*B*.

B. Structural order parameter in the real space. Next, we discuss the structural order parameter in real space, obtained from the radial distribution function (RDF) $g(r)$. The average RDF for two different densities is shown in Fig. S2*A*. The peaks of RDF increase as we go to higher densities. We can rewrite the expression for the depth of the potential, Eq.5, in real space for a bidisperse system as

$$\beta \Phi_r^{\mathrm{av}}(\Delta r = 0) = -\rho \int \mathbf{dr} \sum_{u=1}^{n} \sum_{v=1}^{n} C_{uv}(r) x_u x_v g_{uv}(r), \quad [6]$$

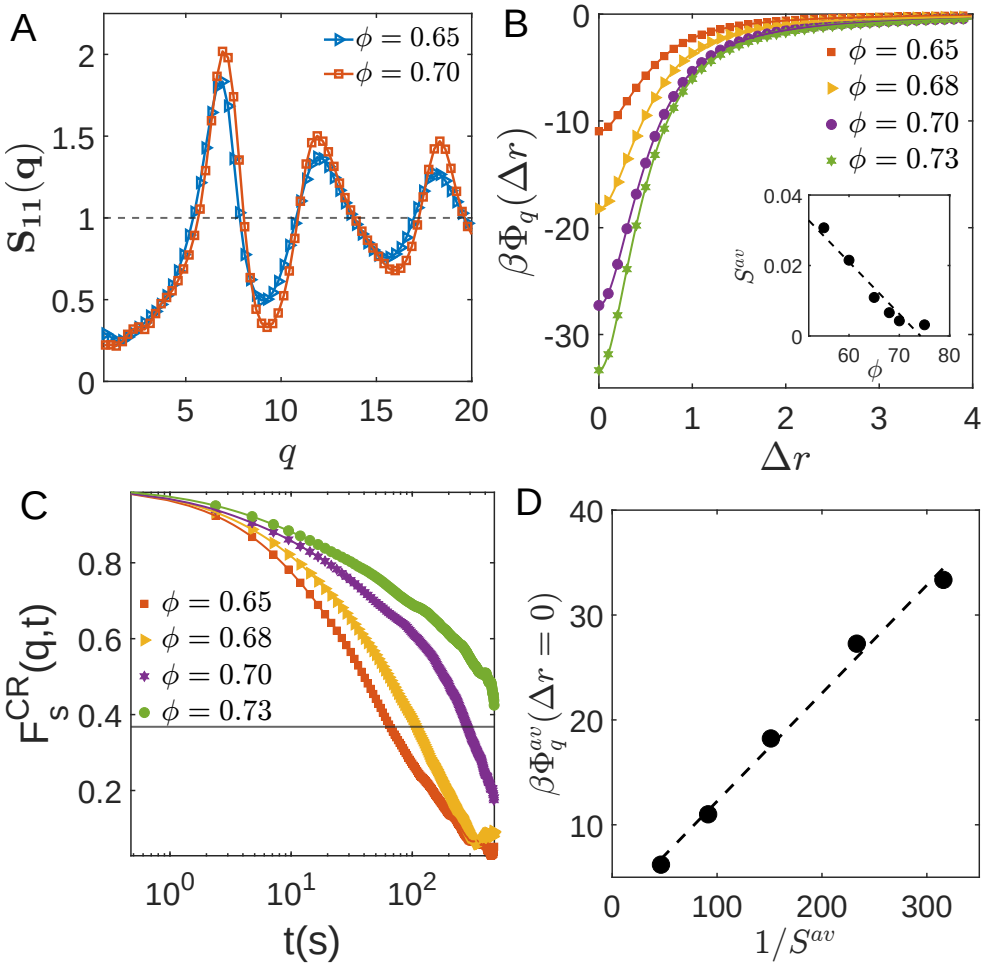

Fig. S1. Global structural order parameter in bidisperse colloidal monolayers. Note that only large particles are considered. (A) The partial structure factor of big particles in a binary colloidal sample at area-fractions $\phi = 0.65, 0.70$. (B) The effective caging potential experienced by the particles for several area fractions. As the area fraction increases, the depth of the potential deepens, and the curvature increases. (C) The intermediate scattering function for several area fractions. With increasing area friction, the relaxation time of the system increases. Relaxation time is obtained from the decay of ISF by a factor of $1/e$, which is shown as a black horizontal line. (D) The scaled depth of the mean field caging potential $\beta\Phi_q(\Delta r = 0)$ in the q space and curvature are determined for several area fractions of the colloidal monolayer. These values are plotted against each other, and the resulting data fit into a linear model represented by the black line.

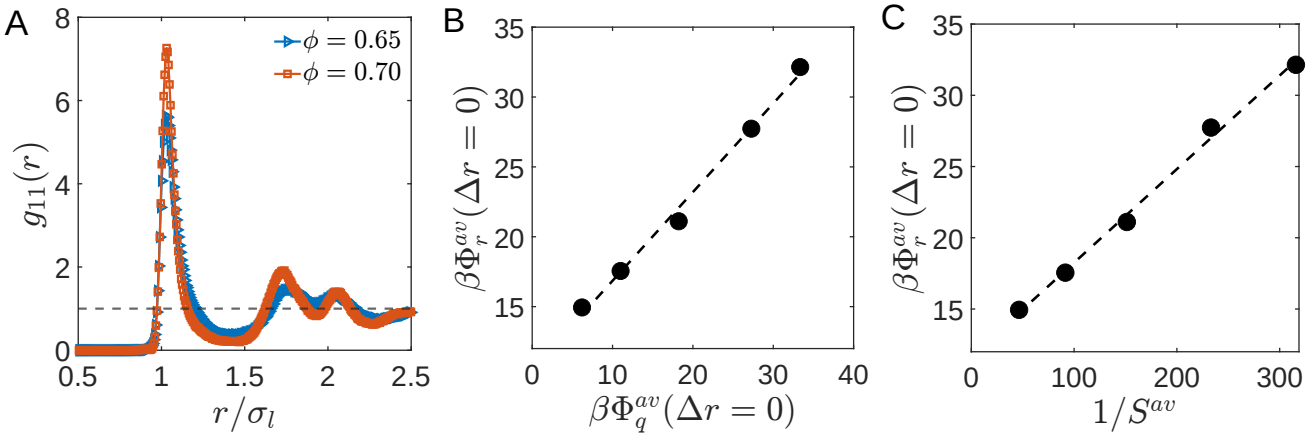

Fig. S2. Global structural order parameter of a bidisperse colloidal monolayer in real space. The results are presented for large particles. (A) Bulk partial pair correlation function at area-fractions $\phi = 0.65,\ 0.70$. (B) The depth of the mean field caging potential in the r plane and in the q plane shows a linear relationship, as depicted by the black line representing a linear fit. (C) The scaled depth of the potential is computed in real space at different system densities, and it is plotted against the inverse of the average SOP value in real space.

where $C_{uv}(r)$ is the partial direct correlation function given by:

$$C_{uv}(r) = -\beta U_{uv}(r) + [g_{uv}(r) - 1] - \ln[g_{uv}(r)]. \quad [7]$$

In the above expression, U_{uv} is the pair interaction potential, which in an experimental setup is unknown a priori. However, it has been shown earlier that replacing $C_{uv}(r)$ by the following equation

$$C'_{uv}(r) \approx [g_{uv} - 1] \quad [8]$$

marginally improves the predictive power of the order parameter (6). Further discussion on this point is presented in the next section. Thus, in our calculation of the caging potential, we replace $C_{uv}(r)$ by $C'_{uv}(r)$. Fig. S2*B* shows that the depth of the potential in the q-plane $\beta\Phi_q^{\rm av}(\Delta r = 0)$ and in the r-plane $\beta\Phi_r^{\rm av}(\Delta r = 0)$ vary linearly. Furthermore, the scaled depth of the potential $\beta\Phi_r^{av}(\Delta r = 0)$ and the curvature of the caging potential obtained from q-space are linearly related as shown in Fig. S2*C*. This implies that the structural order parameter in real space is the inverse of the depth of the caging potential *i.e.*, $S^{av} = \frac{1}{|\beta\Phi_r^{av}(\Delta r=0)|}$.

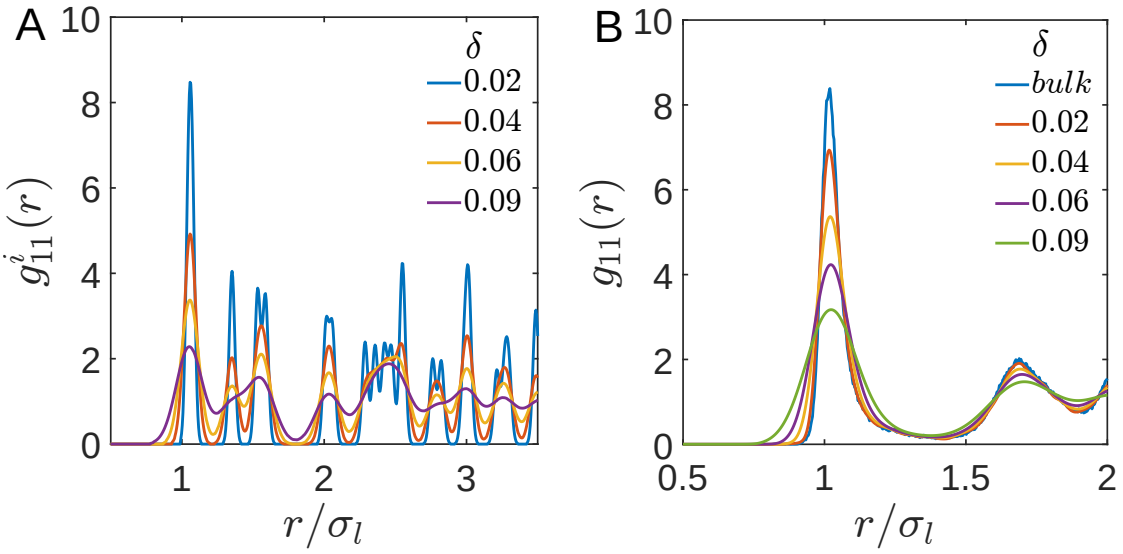

Fig. S3. (A) Partial particle level $g^i(r)$ for a representative particle of type 1 for various values of broadening parameters. (B) Bulk partial $g(r)$, which is averaged over all particles, for different broadening parameters for type 1 particles.

C. Calculation of local structural order parameter. The method of deriving a structural order parameter from the structure factor was extended to the local particle level by Sharma and Bhattacharyya (3). While it is challenging to determine the structure factor $\mathbb{S}(\mathbf{q})$ at the particle level, one can obtain a particle level $g^i(r)$ using a mollified version given by the following expression (3, 7)

$$g_{uv}^i(r) = \frac{1}{\rho_v \mathbf{dr}} \sum_j \frac{1}{\sqrt{2\pi\delta^2}} \mathrm{e}^{-\frac{(r - r_{ij})^2}{2\delta^2}}, \quad [9]$$

where $\mathbf{dr} = 2\pi r dr$ is the annular area in two-dimensions and annular volume $4\pi r^2 dr$ in three-dimensions, ρ_v denotes the density of neighbors, r represents the distance from the tagged particle, r_{ij} represents the distance between tagged particle i and its neighbors j and δ is the broadening parameter. The mollification is crucial to ensure that the derivatives of $g^i(r)$ remain continuous. This leads to the following expression for caging potential for type 1 at the particle level in real space:

$$\beta\Phi_r^i(1, \Delta r = 0) = -\rho_v \int \mathbf{dr} \sum_{v=1}^{2} x_v C'^i_{1v} g^i_{1v}(r), \quad [10]$$

choosing an optimum value for δ is crucial; for small values, $g(r)$ becomes discontinuous, while higher values tend to smear out local information. In our calculations, we selected $\delta = 0.06$ for the $2D$ binary system and $\delta = 0.02$ for the $3D$ system. The impact of the broadening factor is shown in Fig. S3*A* at a particle level and in Fig. S3*B* at a bulk level by averaging over all particles. The integral is numerically calculated using Simpson's rule up to a cutoff distance r_{max}, which corresponds to the first minimum of $g(r)$.

With this understanding of the particle-level radial distribution function (RDF), we can now explain why C'_{uv} in Eq.8 is used to determine the caging potential, instead of $C_{uv}(r)$ in Eq.7. The calculation of $\beta\Phi_r^i(\Delta r = 0)$ in Eq.10 involves the

product of particle level RDF and the direct correlation function. This leads to a term that is the product of RDF and the pair interaction potential $U_{uv}(r)$. The particle level RDF, due to the Gaussian approximation, has finite values at distances smaller than the average RDF (3). Due to this finite value of the RDF at small r, its product with any interaction potential, which diverges at small r, leads to a large unphysical contribution from this range. Thus, in our calculation of the caging potential, we replace $C_{uv}(r)$ by $C'_{uv}(r)$. This was shown to give better prediction for repulsive WCA system, as well as attractive Lennard-Jones system (6). We exploits these findings to calculate the caging potential of colloidal suspensions where the interparticle interactions are unknown.

We next compute the depth of the local caging potential, $|\Phi^i_r(\Delta r = 0)| = \Phi^i$ (Eq.1 in the main text). The inverse depth of the caging potential is the structural order parameter.

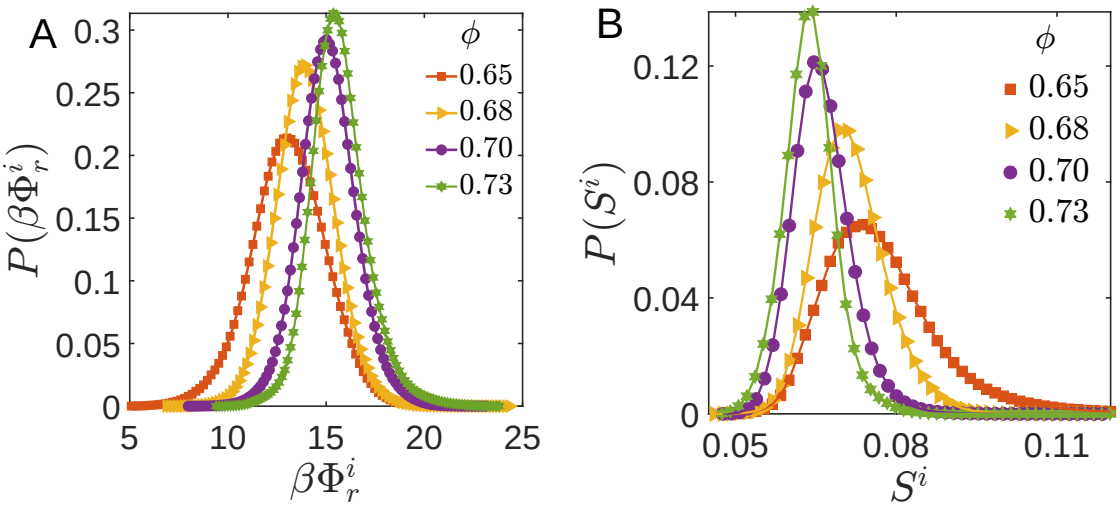

Fig. S4. Distribution of local caging potential(A) and SOP(B) with increasing area-fraction for a bidisperse colloidal monolayer. The distributions are computed using the coarse-grained caging potential. A cut-off distance L corresponding to the second minima of the pair function is used.

The SOP presented in the main paper is obtained from the coarse-grained values of the depth of the potential. The coarse-graining method followed is given by the following expressions

$$\Phi^i_{CG} = \frac{\sum_j \Phi^j f(r_{ij}, L) + \Phi^i}{\sum_j f(r_{ij}, L) + 1}, \quad [11]$$

where $f(r_{ij}, L)$ is the switch function with a cutoff L (7, 8). The switch function ensures a value of 1 for $r_{ij} << L$, 0 for $r_{ij} >> L$, and its functional form is given by:

$$f(r_{ij}, L) = \frac{1 - (r_{ij}/L)^N}{1 - (r_{ij}/L)^M}, \quad [12]$$

where $N = 6$, $M = 12$, and the cutoff $L = 2$ in units of σ_l, which is the diameter of the large particles and set to unity. The value of $L = 2$, unless specified explicitly. We adopt this procedure to coarse-grain the local caging potential, and the resulting distributions of SOP are shown in Fig. S4. There is a clear distinction between the distribution as the density of colloids in the monolayer varies. Note that L was set to the second nearest neighbour shell both in two and three dimensions for amorphous systems. Thus the particle level SOP, $S^i \propto \frac{1}{\Phi^i_{CG}}$.

2. Structural order parameter of rearranging particles in bidisperse colloidal monolayer

We assess the predictive power of the order parameter for rearrangement. In Fig. S5, we compare the distributions of SOP of all particles $P(S^i)$ and the rearranging particles $P(S^i|R)$ at different densities $\phi = 0.65$ and 0.70. It is observed that the particles undergoing rearrangements have a higher SOP or a smaller depth of local caging potential. This difference is more pronounced at higher densities. The shaded area represents the fraction of rearranging particles with SOP higher than the peak of the bulk distribution. This fraction is 72% in Fig. S5*A* and 89% in Fig. S5*B*.

3. Structural order parameter dependent probability of rearrangements.

A. Comparison of different methods used for calculating P_R. Two methods for calculating $P_R(S)$ were described in section H of Material and Methods in the manuscript - Fisher-Yates shuffle algorithm and slicing algorithm. Fig. S6 illustrates comparison of the two methods. The rearrangements are identified over a timescale $\tau_r = 100s$ and a cutoff on relative displacements

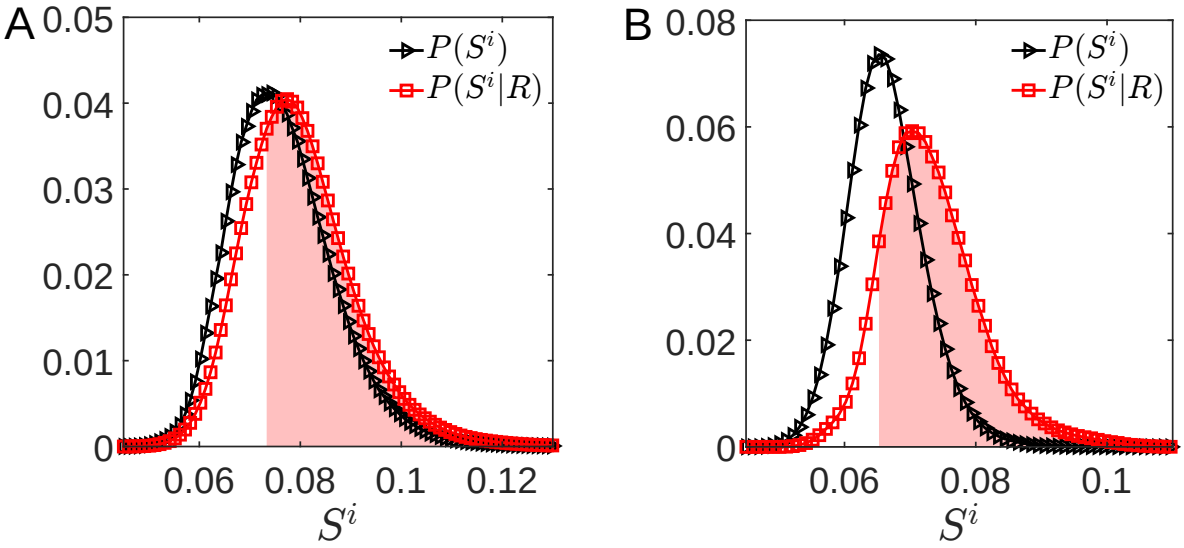

Fig. S5. Distribution of SOP of all particles(circles) and the rearranging particles(squares) in a bidisperse colloidal monolayer. The area-fractions are $\phi = 0.65$ (A) and $\phi = 0.70$ (B). The rearrangements were determined from the relative displacements of particles with respect to a reference configuration. The shaded area represents the fraction of rearranging particles with SOP higher than the peak of the bulk distribution. This fraction is 72% in (A) and 89% in (B).

$l_r^2 = 0.25$. The colour markers with the error bars show the P_R when the system is sliced into 22 different time steps, and each slice gives one P_R whose mean and standard deviations are plotted. The black dashed line represents the P_R when calculated using the Fisher-Yates algorithm considering 100 random configurations, each consisting of 5% of the total particles. The marker symbols represent the data obtained from slicing algorithm. We find that, apart from the tails at high densities, where there are fewer rearrangements and thus poorer statistics, the mean values of $P_R(S)$ in both the data sets match. Since the former method allows us to average over 100 configurations, we get better statistics and smaller error bars.

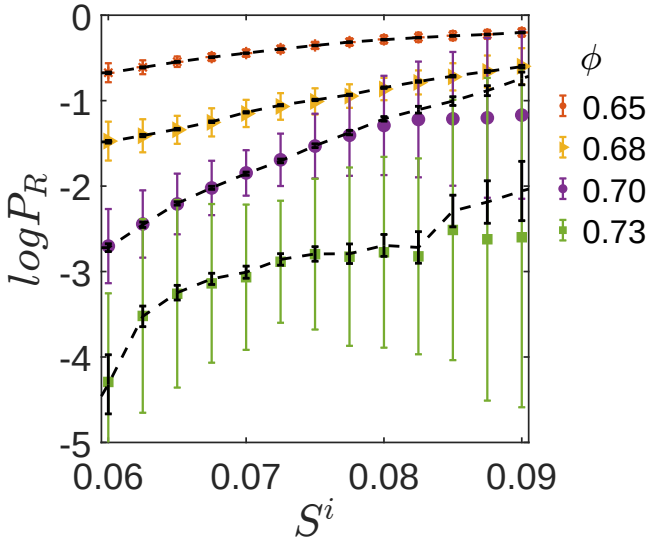

Fig. S6. The rearrangement probability, $P_R(S)$, with error bars equal to the standard deviation. The colour markers with the error bars show the P_R when the system is sliced into 22 different time steps, and each slice gives one P_R whose mean and standard deviations are plotted. The black dashed line represents the P_R when calculated using the Fisher-Yates algorithm considering 100 random configurations, each consisting of 5% of the total particles.

B. $P_R(S)$ for full range of SOP values . The individual curves of $P_R(S)$ for $\phi = 0.65$ and 0.70 are presented in Fig. S7A and Fig. S7B over an extended range of S values. The error bars are large, and the statistics are poor. The other observation is that the $P_R(S)$ saturates beyond a threshold value of S, which is clear from the low area-fractions data. This implies that beyond a critical value of SOP, nearly all the particles rearrange, and $P_R(S)$ becomes independent of S.

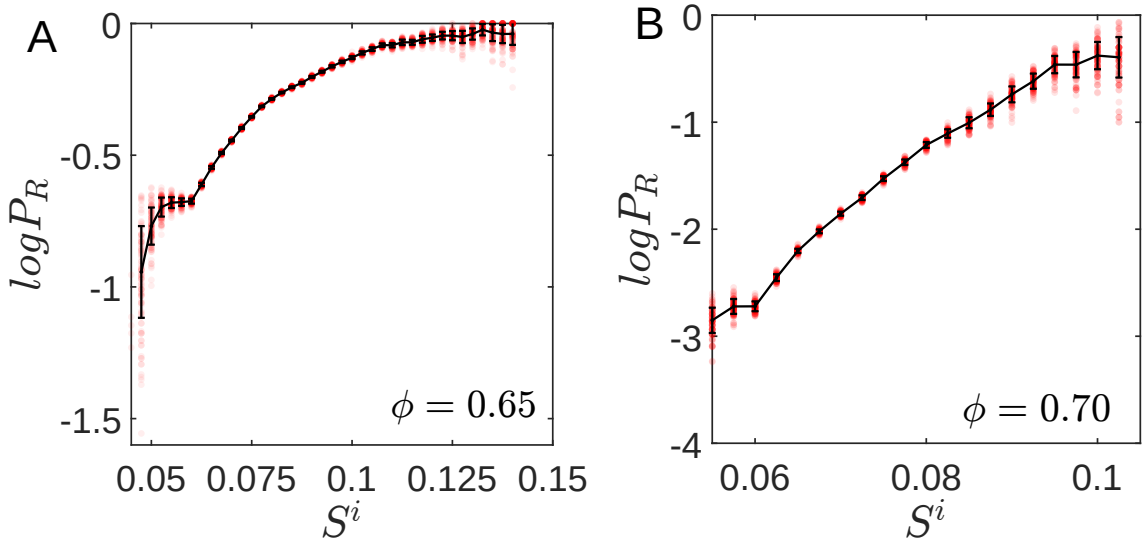

Fig. S7. The rearrangement probability P_R for two area-fractions $\phi = 0.65$ (A) and $\phi = 0.70$ (B) are shown separately over the full range of S values. The error bars are equal to standard deviation and the red circles show scatter of data points. Fisher-Yates shuffle algorithm was used for $P_R(S)$ calculations.

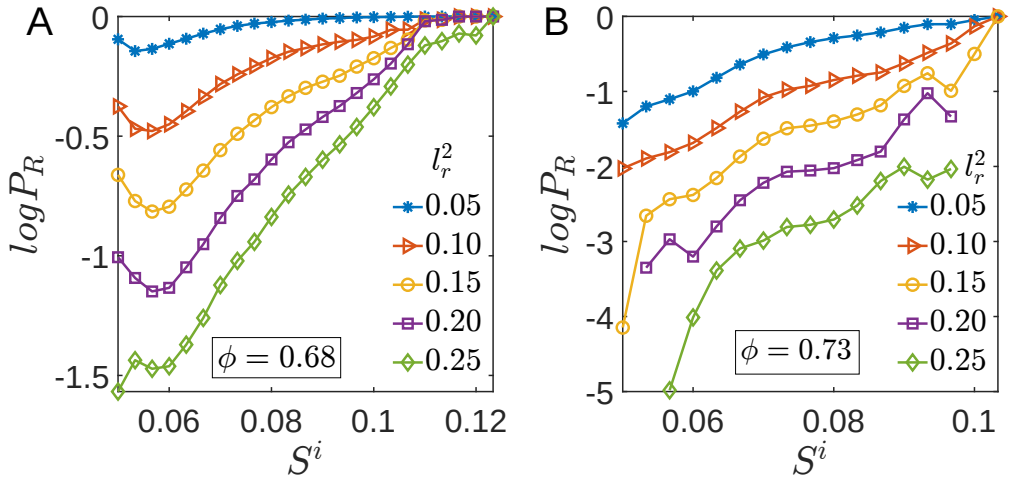

Fig. S8. The rearrangement probability $P_R(S)$ at $\phi = 0.68$ (A) and $\phi = 0.73$ (B) are presented for various values of the cutoff threshold l_r^2.

C. Effect of thresholding on $P_r(S)$ in quiescent systems. The threshold parameters in quiescent system are the timescale τ_r and the length-scale l_r. Varying these parameters changes the form of $P_R(S)$. The Fig. S8A and Fig. S8B presents the rearrangement probability at $\phi = 0.68$ and 0.73, respectively, for varying cutoff l_r. Note that l_r is the displacement cutoff and all particles with $d_i^2 > l_r^2$ are considered as rearranging. The timescale used in these calculations is $\tau_r = 100s$. What is clear from these figures is that $P_R(S)$ saturates at a smaller value of S with decreasing l_r. This implies that all particles above a certain value of S undergo rearrangement, leading to saturation of P_R.

A similar effect is seen with increasing timescale τ_r, which are presented in Fig. S9A and Fig. S9B for $\phi = 0.68$ and $\phi = 0.73$, respectively. These calculations are done using a cutoff of $l_r^2 = 0.25$.

D. Effect of thresholding on $P_r(S)$ in sheared systems. We have checked the effect of threshold to identify the rearrangements in the sheared system by varying the cutoff D_r^2 as well as the $\Delta\gamma_r$. These results are displayed in Fig. S10A and Fig. S10B, respectively. It is observed that increasing $\Delta\gamma_r$ or lowering D_r^2 leads to early saturation of $P_R(S)$, implying that "rearrangements" occur even in the regions of lower S.

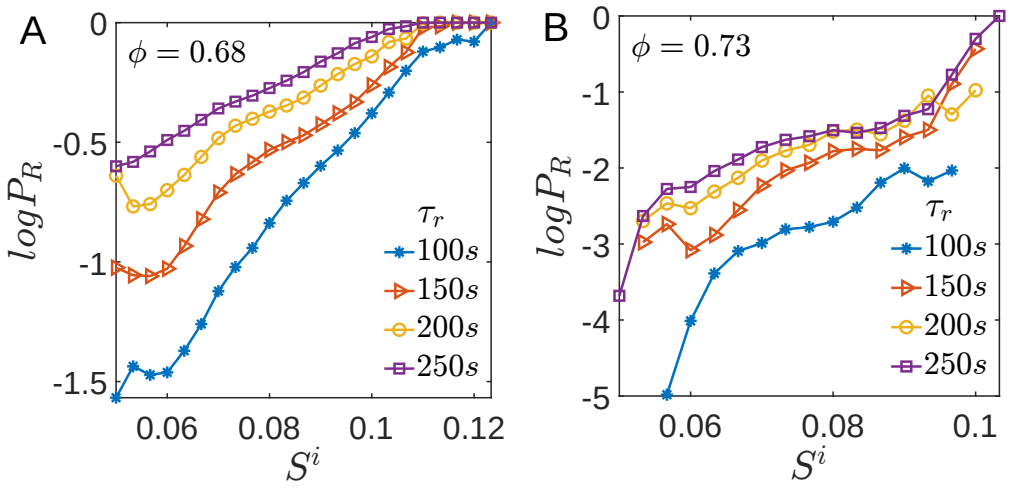

Fig. S9. P_R with $l_r^2 = 0.25$ and the time scale to calculate the relative displacements is varied(A) for area fraction $\phi = 0.68$ and (B) $\phi = 0.73$.

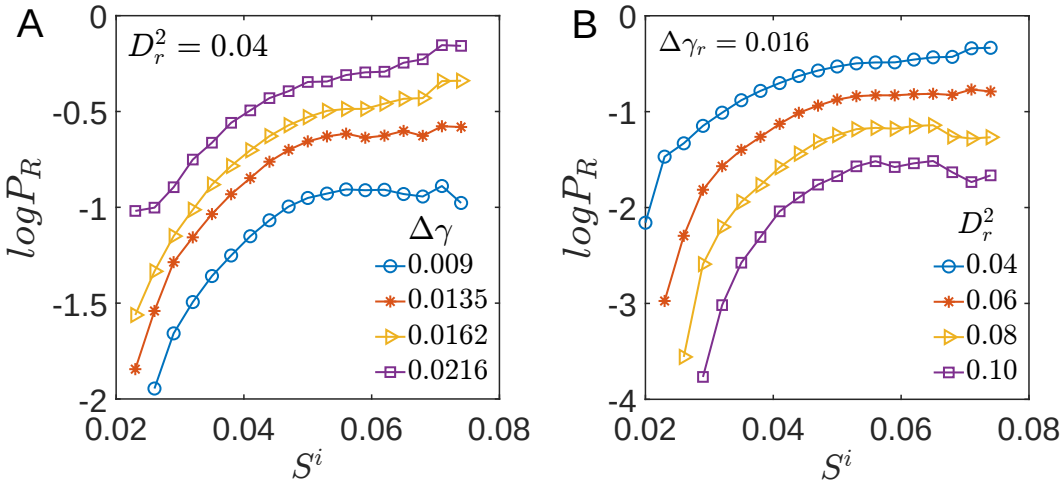

Fig. S10. P_R with varying the $\Delta\gamma_r$ for a fixed cutoff of $D_r^2 = 0.04$(A) and P_R as a function of cutoff for $\Delta\gamma_r = 0.0162$.

4. Structure-dynamics correlations using Spearman rank correlation coefficient

A. Spearman rank correlations of quiescent system and effect of coarse-graining SOP. To calculate the Spearman rank correlation coefficient, we have considered the larger species only. The method is discussed in the section I of Materials and Methods. The Fig. $2F$ in the main part shows a Spearman correlation coefficient with a maximum value of ~ 0.46 for $\phi = 0.73$.

Previous studies (3, 6, 9–12) have shown that varying the coarse-graining length, L, used for determining the SOP (Eq.11) leads to improved correlations. This is demonstrated in Fig. S11C for $\phi = 0.73$, where the correlation coefficient increases to ~ 0.5 at L=4. We also observe that the highest L value where the rank correlation is maximum changes with the density. With increasing density, the value of L increases. This is because the cooperatively rearranging regions grow with density. We elucidate these points in Fig. S11A-C, where the SCC has been presented for $\phi = 0.68$, 0.70, and 0.73, respectively, for various coarse-graining lengths L. Evidently, SCC attains an maximum value at $L = 2$ for $\phi = 0.68$, at $L = 3$ for $\phi = 0.70$ and at $L = 4$ for $\phi = 0.73$.

5. Scatter plots of SOP and particle displacements

We present the scatter plot of the SOP values and the relative displacements for the quiescent system at densities $\phi = 0.68$ and 0.73 in Fig. S12A and Fig. S12B, respectively, for the big particles.

Scatter plot of SOP and the non-affine displacements for the sheared system in the steady state at $\gamma = 0.614$ is presented in Fig. S13. The non-affine displacements are computed over a timescale of $\Delta\gamma_r$ and the SOP is coarse-grained using $L = 2$ (A)

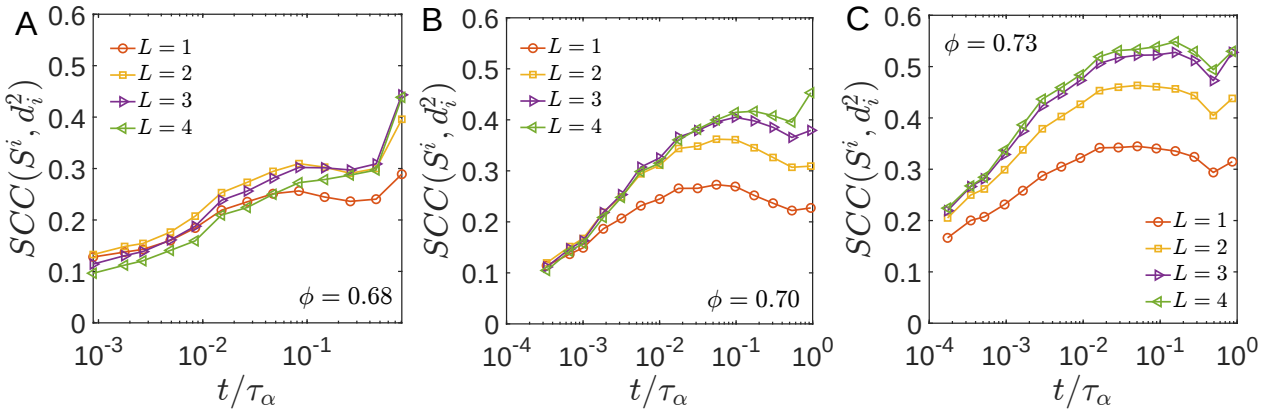

Fig. S11. Spearman rank correlation of SOP and relative displacement for different area fractions as a function of coarse-graining length scale. This is to support the growth of CRR.

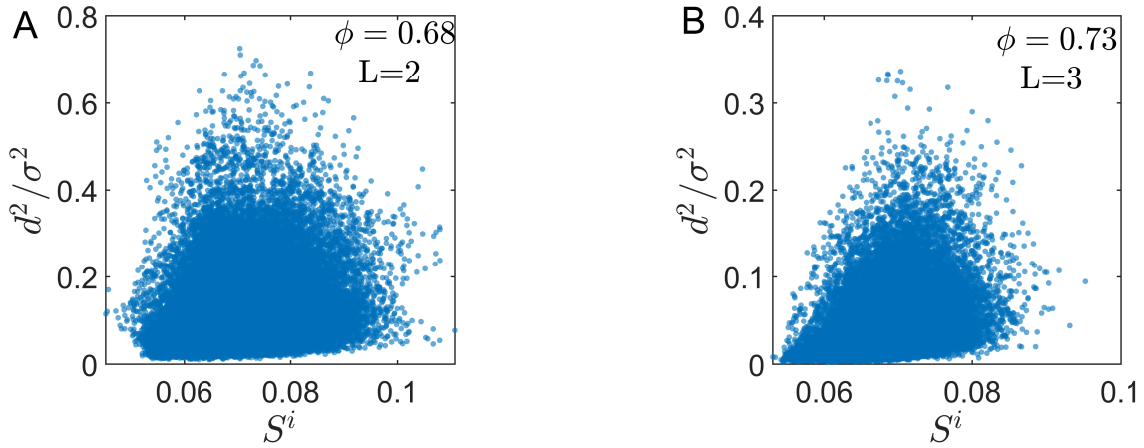

Fig. S12. Scatter plot for $\phi = 0.68$(A) and $\phi = 0.73$(B) for $\Delta t = 100s$. The coarse-graining length L is denoted in the figure panels.

and $L = 3$ (B).

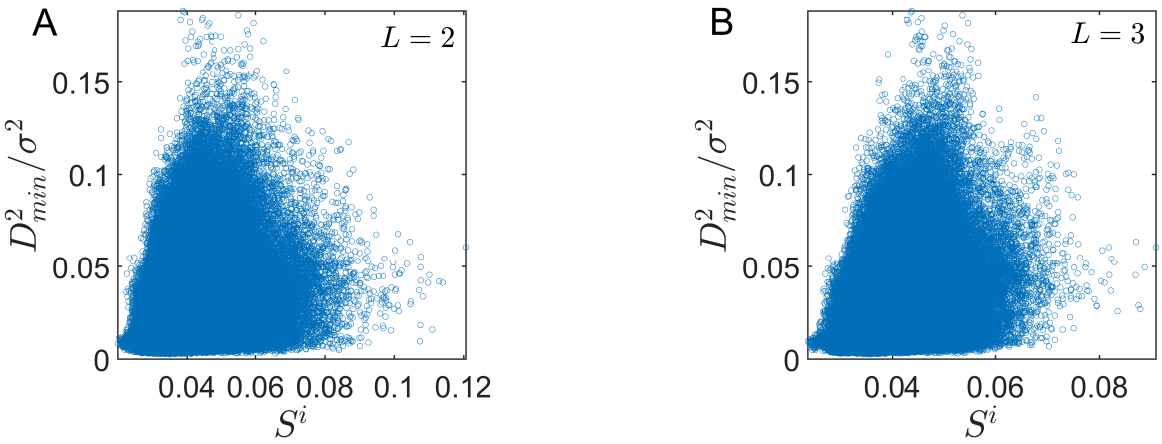

Fig. S13. Scatter plot of SOP and the non-affine displacements in the steady state at $\gamma = 0.614$. The non-affine displacements are computed over a strain interval $\Delta\gamma_r$ and the SOP is coarse-grained to $L = 2$ (A) and $L = 3$ (B).

6. Structure and dynamics in sheared systems in 3D

Fig. S14*A* depicts the changes in the radial distribution function and Fig. S14*B* shows the average non-affine displacements $\bar{D}^2_{min}(\gamma, \Delta\gamma)$ due to the applied strain at $\dot{\gamma} = 1.5 \times 10^{-5} s^{-1}$ in the left and right panels, respectively. The peak of $g(r)$ decreases with increasing strain and ceases to show variations when the system reaches a steady state. Similarly, the dynamics represented by $\bar{D}^2_{min}(\gamma, \Delta\gamma)$ do not show appreciable variations with γ in the steady state. The magnitude of $\bar{D}^2_{min}(\gamma, \Delta\gamma)$ in the transient stages of deformation, corresponding to $\gamma = 0.009$ and 0.046, is considerably smaller than the steady state after $\gamma = 0.221$. This is due to fewer particle rearrangements in the early stages of deformation over a comparable strain interval $\Delta\gamma$.

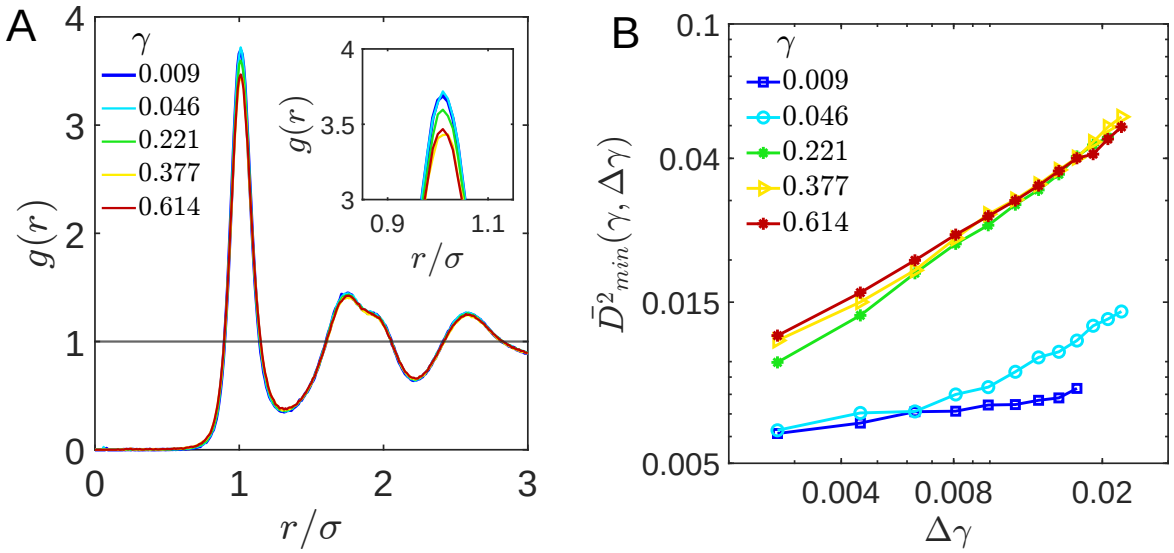

Fig. S14. Structure and dynamics at a shear-rate $\dot{\gamma} = 1.5 \times 10^{-5} s^{-1}$. (A) The radial distribution function $g(r)$ of the system at several strain values. (B) The average non-affine displacement $\bar{D}^2_{min}(\gamma, \Delta\gamma)$ as a function of applied strain.

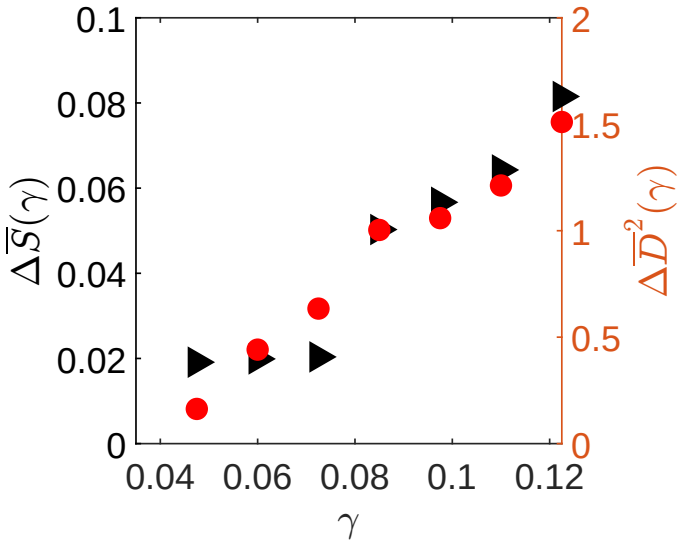

Fig. S15. Structure and dynamics at a shear-rate of $\dot{\gamma} = 10^{-4} s^{-1}$ Scaled change in mean structural order parameter, $\Delta\bar{S}$(triangle symbol) and that of non-affine displacement $\Delta\bar{D}^2$(circle symbol) as the system is strained.

Fig. S15 shows the variation in average SOP $\bar{S}(\gamma)$ and average non-affine displacements $\bar{D}^2(\gamma)$ due to the applied strain γ at a strain-rate of $\dot{\gamma} = 10^{-4} s^{-1}$. The scaled change in average SOP $\Delta\bar{S}(\gamma) = \frac{\bar{S}(\gamma) - \bar{S}(\gamma_0)}{\bar{S}(\gamma_0)}$, where the bar represents averaging over all particles, and the angular bracket denotes averaging over multiple configurations is shown on the left axis using triangle symbols. Similarly, the scaled change of average non-affine displacement $\Delta\bar{D}^2(\gamma) = \frac{\bar{D^2}_{min}(\gamma, \gamma_0) - \bar{D^2}_{min}(0, \gamma_0)}{\bar{D^2}_{min}(0, \gamma_0)}$, is presented on the right side of the vertical axis using circle symbols. Note the bar denotes the average over all particles, and $\gamma_0 = 0.0025$ represents the smallest strain interval considered in our study.

References

1. MK Nandi, A Banerjee, C Dasgupta, SM Bhattacharyya, Role of the pair correlation function in the dynamical transition predicted by mode coupling theory. *Phys. Rev. Lett.* **119**, 265502 (2017).
2. MK Nandi, SM Bhattacharyya, Microscopic theory of softness in supercooled liquids. *Phys. Rev. Lett.* **126**, 208001 (2021).
3. M Sharma, MK Nandi, SM Bhattacharyya, Identifying structural signature of dynamical heterogeneity via the local softness parameter. *Phys. Rev. E* **105**, 044604 (2022).
4. T Ramakrishnan, M Yussouff, First-principles order-parameter theory of freezing. *Phys. Rev. B* **19**, 2775 (1979).
5. KS Schweizer, Derivation of a microscopic theory of barriers and activated hopping transport in glassy liquids and suspensions. *The J. Chem. Phys.* **123**, 244501 (2005).
6. M Sharma, MK Nandi, S Maitra Bhattacharyya, A comparative study of the correlation between the structure and the dynamics for systems interacting via attractive and repulsive potentials. *The J. Chem. Phys.* **159** (2023).
7. PM Piaggi, O Valsson, M Parrinello, Enhancing entropy and enthalpy fluctuations to drive crystallization in atomistic simulations. *Phys. Rev. Lett.* **119**, 015701 (2017).
8. PM Piaggi, M Parrinello, Entropy based fingerprint for local crystalline order. *The J. chemical physics* **147**, 114112 (2017).
9. H Tong, H Tanaka, Structural order as a genuine control parameter of dynamics in simple glass formers. *Nat. communications* **10**, 5596 (2019).
10. H Tong, H Tanaka, Revealing hidden structural order controlling both fast and slow glassy dynamics in supercooled liquids. *Phys. Rev. X* **8**, 011041 (2018).
11. H Tong, H Tanaka, Role of attractive interactions in structure ordering and dynamics of glass-forming liquids. *Phys. Rev. Lett.* **124**, 225501 (2020).
12. J Paret, RL Jack, D Coslovich, Assessing the structural heterogeneity of supercooled liquids through community inference. *The J. chemical physics* **152** (2020).